Artifact analysis of approximate helical cone-beam CT reconstruction algorithms

Th. Köhler,[a] R. Proksa, C. Bontus, and M. Grass
Philips Research Laboratories, Sector Technical Systems, Roentgenstrasse 24-26, D-22335 Hamburg, Germany

J. Timmer
Philips Medical Systems, Vennpluis 4-6, 5680 DA Best, The Netherlands

(Received 2 May 2001; accepted for publication 4 September 2001; published 26 December 2001)

In this paper, four approximate cone-beam CT reconstruction algorithms are compared: Advanced single slice rebinning (ASSR) as a representative of algorithms employing a two dimensional approximation, PI, PI-SLANT, and 3-PI which all use a proper three dimensional back-projection. A detailed analysis of the image artifacts produced by these techniques shows that aliasing in the *z*-direction is the predominant source of artifacts for a 16-row scanner with 1.25 mm nominal slice thickness. For a detector with isotropic resolution of 0.5 mm, we found that ASSR and PI produce different kinds of artifacts which are almost at the same level, while PI-SLANT produces none of these artifacts. It is shown that the use of redundant data in the 3-PI method suppresses aliasing artifacts efficiently for both scanners. © *2002 American Association of Physicists in Medicine.*
[DOI: 10.1118/1.1413518]

Key words: cone-beam CT, cone-beam reconstruction, helical CT, PI, PI-SLANT, *n*-PI, ASSR

I. INTRODUCTION

The introduction of multi-slice CT systems offers a couple of benefits. Compared to a single slice CT system, the time for data acquisition can be reduced, the output of the x-ray tube is used more efficiently leading to a simpler heat management of the tube, and there is no longer the need for compromising *z*-resolution in order to achieve an acceptable scan time. However, a major problem using multi-slice CT systems is to find a proper reconstruction algorithm. A large number of publications within the last few years have addressed the problem of the reconstruction of cone-beam projections acquired during a helical path of the source–detector system. For a small number of detector rows, the cone-angle can be simply ignored without loss of image quality, and corresponding reconstruction algorithms can be used.[1–3] For large cone-angles, exact methods might be necessary as, e.g., radon inversion or 3D back-projection of projections after sophisticated preprocessing.[4–7] There is also great interest in approximate methods that take into account the cone-angle to address the segment of medium cone angles. We would like to partition these algorithms into two classes: The first class performs a two dimensional reconstruction on slices that fit locally to the helical path.[8–12] It has been shown that these methods yield superior image quality compared to 2D techniques based on slices perpendicular to the rotation axis. The second class performs a proper 3D back-projection of pre-processed data.[13–15] Of course, the 3D back-projection is computationally much more demanding. A major question is whether the image quality becomes significantly better compared with 2D techniques to justify the additional effort.

Another important question is whether it is useful to take redundant data into account. Proksa *et al.* [15] introduced the 3-PI data acquisition, in which all object points are illuminated over an angular range of 540°. It was shown that in combination with the 3-PI filtered back-projection algorithm, a significant improvement in image quality compared to the PI-method can be achieved. Most of the 2D techniques cannot handle redundant data apart from a small over-scan. Recently, the extended single slice rebinning (ESSR) algorithm was published by Bruder *et al.* [11] which is also capable of handling redundant data. It is an extended version of the advanced single slice rebinning (ASSR) algorithm by Kachelrieß *et al.* [10] However, if the table feed is reduced by a factor of two compared with the maximum pitch for ASSR, it appears that ''the image quality of the ESSR algorithm is slightly reduced.'' [11] Most recently, Schaller *et al.* presented another modification of ASSR, named advanced multi planar reconstruction (AMPR).[16] This method is also capable of handling redundant data and produces—in contrast to ESSR—better image quality, if redundant data are taken into account.

In this paper, we compare four approximate reconstruction methods: ASSR,[10] PI,[17,18] PI-SLANT,[14] and the filtered back-projection version of 3-PI[15] (we will refer to this method as to the 3-PI method). This selection is motivated by the following consideration: PI, PI-SLANT, and 3-PI use a proper 3D back-projection during reconstruction. The main difference between PI and PI-SLANT is the filter direction. In PI-SLANT, this filter direction is chosen such that line integrals related to rays passing through a certain set of object points are always filtered together as well as possible. In ASSR as well as in the algorithms proposed by Larson *et al.*[8] and Heuscher,[9] 2D sinograms are produced by a similar procedure, and a 2D back-projection is performed on 2D planes which locally fit to the helix. We chose ASSR for this comparison study because it is well documented and because

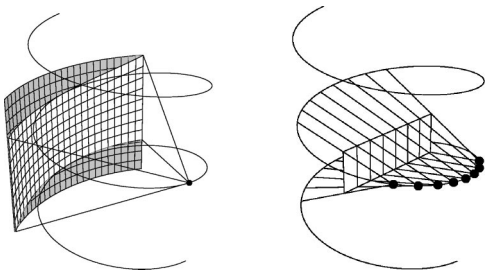

FIG. 1. Left: Detector area used for the PI- and the PI-SLANT method. Only the white area of the focus centered detector is used. Right: System geometry after parallel rebinning.

it was stated last year, that ''ASSR, compared with other approximate cone-beam reconstruction algorithms, is the most promising method available today.'' [19]

II. METHOD

We shortly describe the main tasks to be done for each reconstruction algorithm under consideration. The x-ray source moves on a helical path,

$$S(\lambda)=(-R\sin\lambda,-R\cos\lambda,\lambda P/2\pi), \tag{1}$$

around the object. The pitch P is the table travel per rotation and R the radius of the helix. A focus-centered detector at distance L from the x-ray source is used throughout this paper.

A. The PI method

The PI method,[17,18] also called the original PI method, is based on a special measurement geometry that provides sufficient and nonredundant data. This measurement geometry is shown on the left hand side of Fig. 1. The reconstruction is based on a parallel rebinning and a 3D back-projection. The geometry after rebinning is shown on the right hand side of Fig. 1. The virtual detector is a perfect rectangle. For details of the reconstruction algorithm, we refer to the original work by Danielsson *et al.* [17] and Turbell.[18]

B. The PI-SLANT method

This method is a variation of the PI method and is motivated by the following observation: A set of object points that enters the cone of rays at a common point in time also leaves the cone at a common point in time. For these two discrete time points, this set of object points is projected onto the lower and upper boundary of the virtual detector. If these object points were projected onto a line or at least a one dimensional curve during the whole data acquisition, the line integrals which contribute to these curves would be computed only from these object points and consequently, it would be possible to put them into 2D sinograms and to perform an exact reconstruction. As a matter of fact, this set of object points is projected onto a one dimensional curve only for the two discrete time points mentioned earlier. Figure 2 shows, how a couple of these points are projected onto the virtual detector during the illumination. The main idea of PI-SLANT is to adjust the filter direction in a way that line integrals which are produced by object points that enter and leave the cone together are filtered always together as well as possible. Turbell proposed to use the lines[14]

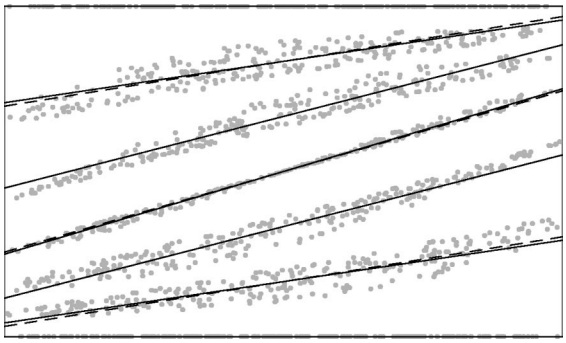

FIG. 2. Projection of a set of object points that leave and enter the cone at the same time for some discrete time points. The main idea of the PI-SLANT method is to adjust the filter direction in a way that these points are filtered always together as well as possible. The filter lines proposed by Turbell are indicated by solid lines, while the filter lines used in this paper are plotted as dashed lines.

$$v(l,u)=l-u\frac{P}{4R\sqrt{1+\left(1+\left(\frac{P}{4R}\right)^2\right)\tan^2\left(l\frac{2\pi}{P}\right)}}, \tag{2}$$

for constant values $l\in[-P/4{:}P/4]$, where u is the coordinate on the detector perpendicular to the z-axis, v is the coordinate orthogonal to the u coordinate, and l is the line index. During back-projection, l must be determined from u and v, which can be calculated as in the back-projection in the PI method. (Alternatively, the data can be re-sampled after the filtering onto a rectangular grid to allow an easy and fast back-projection. However, this additional interpolation step would introduce an unwanted loss in z-resolution.) One drawback of the definition in Eq. (2) is that this cannot be done analytically. Instead, Turbell proposed to do an iteration to determine l. Here, we approximate the lines by

$$v(l,u)=l-ua\frac{4(l-P/4)(l+P/4)}{PR}, \tag{3}$$

where a is a parameter chosen to be 0.975 to fit the slope defined by Eq. (3) to the original one under the constraint that the slope becomes zero at the lower and upper border of the virtual detector. The resulting filter lines are shown in Fig. 2 together with the lines proposed by Turbell. The deviation is obviously small. Since in this approximation, v depends only quadratically on l, l can be determined analytically from u and v.

C. The *n*-PI method

The n-PI method[15] overcomes the restriction of the PI and the PI-SLANT method that the object points must always be illuminated over 180°. This restriction implies that only a fixed pitch is possible for a given detector. This restriction is somehow relaxed with the introduction of the n-PI method. In the PI method, the used part of the detector is bound by

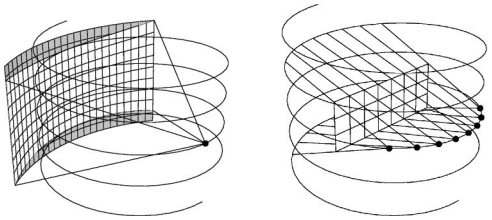

FIG. 3. Left: Detector area used for the 3-PI-method. Only the white area of the focus centered detector is used. Right: System geometry after parallel rebinning.

two successive turns of the helical path of the x-ray source; see Fig. 1. In the *n*-PI method, this window is extended symmetrically by some turns. On the left hand side of Fig. 3, the resulting detector is shown for the case that the window is extended by one turn to both sides, resulting in a 3-PI data acquisition. It is shown in Ref. 15 that this acquisition provides complete data capture. As in the PI-method, reconstruction is done using a parallel rebinning resulting again in a rectangular virtual detector shown on the right hand side of Fig. 3. Details of the algorithm are described in Ref. 15.

D. The ASSR method

Each reconstruction method discussed so far requires a 3D back-projection in the final reconstruction step and is therefore computationally expensive. It has been proposed by several authors to replace the 3D back-projection by a 2D back-projection onto a properly defined 2D slice.[8–10] The definition of this 2D slice aims at minimizing the geometrical error that is made by this assumption. The ASSR method[10] is used here as a representative method for these algorithms.

The 2D slice is defined by minimizing the mean absolute difference between the intersection of the slice with the source cylinder and the source path. The 2D slices nutate around the *z*-axis as shown in Fig. 4.

The final step in ASSR is a *z*-filtering to obtain image data on a rectangular grid. It is proposed by Kachelrieß *et al.* to use an interpolation with a triangle-shaped convolution kernel. The width $\overline{z}$ of the kernel can be used to balance between *z*-resolution and image quality. To reduce interpolation artifact in this last step, a large number of 2D slices has to be reconstructed. The number *w* of slices per nominal slice thickness varies typically between 2 and 5.

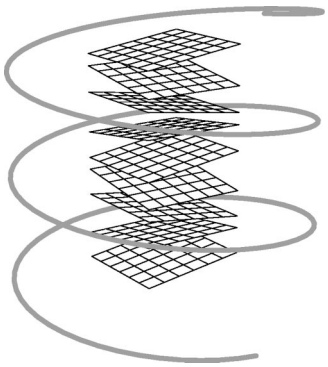

FIG. 4. Schematic view on the 2D slices on which reconstruction is performed in the ASSR method. Each slice fits locally to the helical path of the x-ray source.

TABLE I. Definition of the scanners used in the simulations. *L* is the distance from the source to the detector, *R* the distance of the source to the rotation axis, *H* the detector height, and *P* the table feed per rotation.

	Det16	Det40
# rows	16	40
# columns	900	900
# vertices/turn	1440	1440
L/mm	910	910
R/mm	515	515
H/mm	35.34	35.34
focal spot size/mm^2	1.15×2.875	1.15×1.15
full fan-angle	28.48°	28.48°
cone-angle	2.2°	2.2°
P/mm for short scans	31.382323	31.382323
P/mm for 3-PI	11.508949	11.508949

III. RESULTS

Two scanners with 16 and 40 rows were used for the simulation. The detailed scanner geometry is given in Table I. The 16-row scanner has a nominal slice thickness of 1.25 mm, while the 40-row scanner has a nominal slice thickness of 0.5 mm. Thus, the detector height is the same for both scanners. This choice offers the opportunity to identify artifacts which are produced due to the sampling in the *z*-direction and artifacts produced by the algorithms. The detector is shifted in-plane by a quarter of the pixel width. Note that the fan-angle of the system is unusually small. This is motivated by the fact that the phantom that will be used in the study on image quality is a head phantom.

In order to reduce aliasing, the size of the focal spot of the simulated scanner is chosen in a way that its size projected to the center of rotation is the same as the pixel size projected to the center of rotation.

There is no unique natural way to compare the short-scan methods with the 3-PI method. We distinguish the following approaches.

(i) *Constant-γ*: Here, the cone-angle is kept constant. The given detector area is used as efficiently as possible for each method. This implies that the short scan methods scan a certain field of view in the *z*-direction three times faster than the 3-PI method. If the tube current is kept constant, the signal to noise ratio of the images obtained by the 3-PI method will be larger by a factor of $\sqrt{3}$ compared with the short-scan methods.

(ii) *Constant-pitch*: Here, the pitch is kept constant. The short scan methods use only approximately a third of the detector area. Consequently, the resulting image quality will be higher because the effective cone angle is also reduced by a factor of three. Again, for a constant tube current, 3-PI will provide the larger signal to noise ratio.

(iii) *Constant-dose*: Considering the fast rotation time of

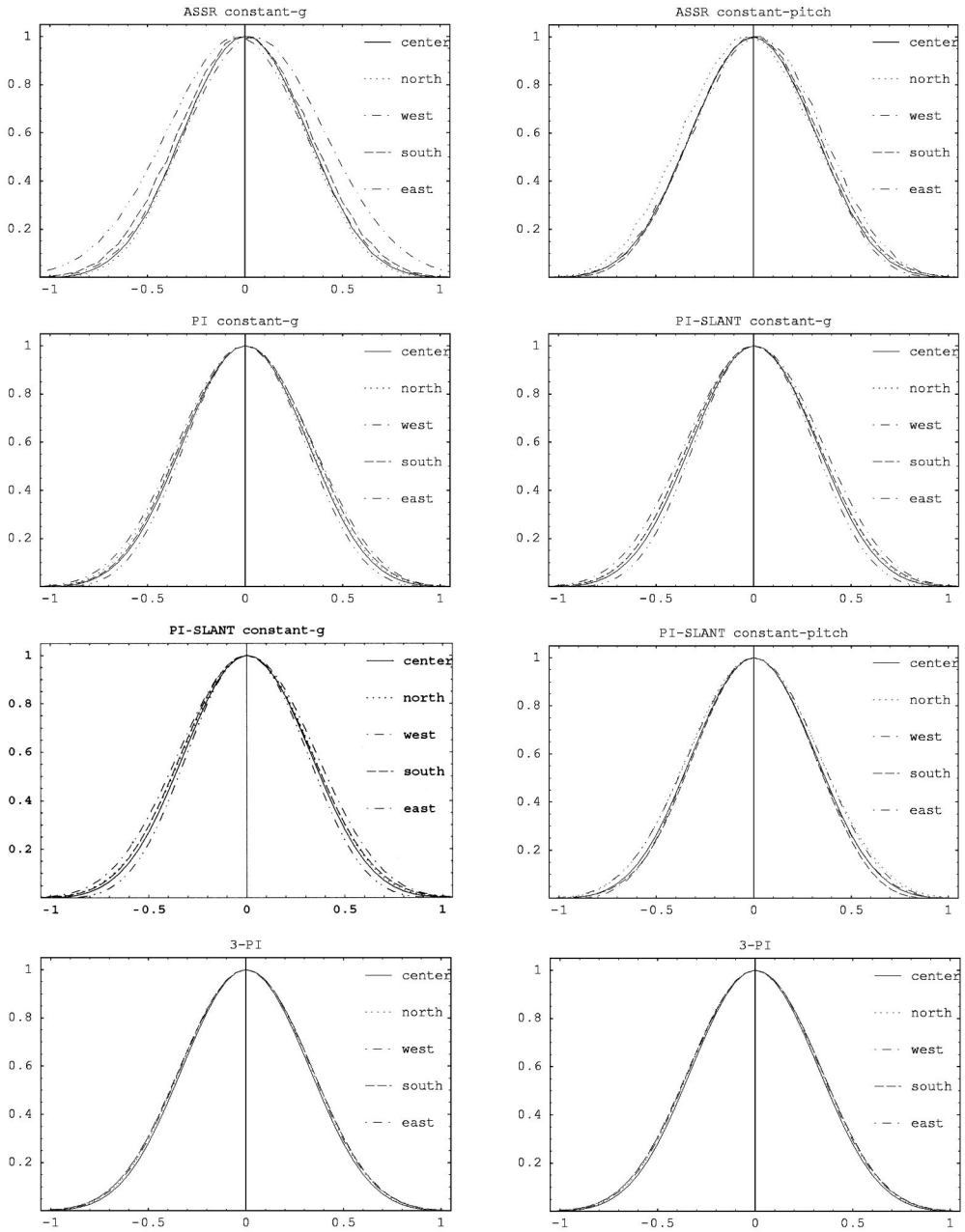

FIG. 5. SSPs obtained by ASSR PI, PI-SLANT, 3-PI using the 40-row scanner. Left: constant-γ comparison, right: constant-pitch comparison.

modern CT-systems, the signal to noise ratio of short scan methods will be sometimes limited by the x-ray tube. In the constant-dose case, the gantry rotation time is reduced by a factor of three for the short scan methods in order to accumulate the same dose as for the 3-PI method while keeping the tube current constant. If the detector has a fixed integration time, the angular sampling is increased by a factor of three.

TABLE II. Effective slice thickness for the 40-row scanner.

	Constant-γ					Constant-pitch				
Method	Center	East	North	West	South	Center	East	North	West	South
ASSR	0.745	0.829	0.723	0.838	0.787	0.745	0.785	0.779	0.746	0.756
PI	0.744	0.712	0.763	0.797	0.774	0.735	0.771	0.777	0.729	0.721
PI-SLANT	0.743	0.705	0.765	0.810	0.767	0.735	0.777	0.782	0.727	0.716
3-PI	0.747	0.765	0.770	0.777	0.774	0.747	0.765	0.770	0.777	0.774

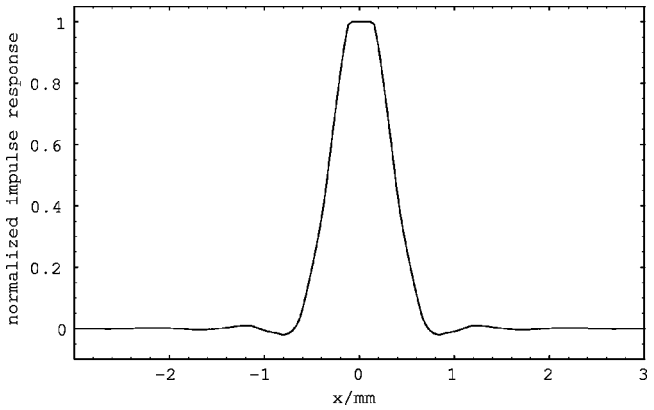

FIG. 6. In-plane PSF obtained by a PI, PI-SLANT, 3-PI, and ASSR reconstruction using the 16-row scanner.

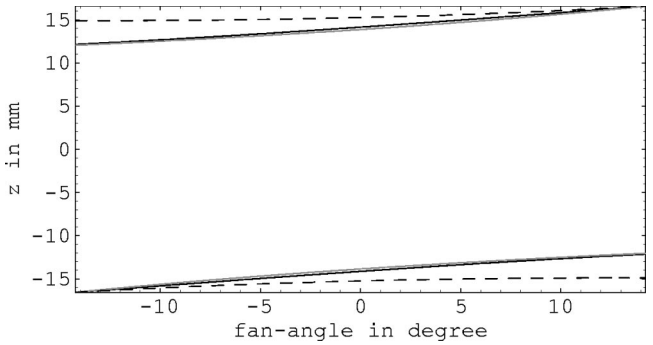

FIG. 7. Detector usage of the different methods in the constant-γ comparison. ASSR (solid black) and PI-/PI-SLANT (solid gray) use almost the same area. The 3-PI method (dashed) uses significantly more of the detector area.

We will carry out the constant-γ and constant-pitch comparisons in detail. The constant-dose comparison is of minor importance because artifacts in the short scan methods are dominated typically by the cone-beam geometry and not by angular sub-sampling. Note that for each comparison mentioned, the 3-PI methods serves as the reference method, i.e., the 3-PI method is used with the same set of parameters.

For the constant-γ comparison, the pitch is the maximum pitch allowed for the PI- and 3-PI-mode, if the 16-row scanner is considered. The 40-row scanner has the same height, but due to the higher number of rows, the maximum allowed pitch would be slightly larger. (During rebinning, an interpolation is performed on the detector area. This interpolation is only possible between the center of the first and the center of the last row. Thus, the area that can be used is one pixel height smaller than the detector height.) However, in order to keep the results of both scanners comparable, we used the same pitch. For the constant-pitch comparison, the 3-PI scan data are used for the short scan methods.

For all reconstructions with the PI, PI-SLANT, and 3-PI method, 6th order Lagrangian interpolation was used in radial and angular direction, while linear interpolation was used in the z-direction. During the resampling step in the z-direction in the constant-γ comparison, the number of detector rows was doubled, i.e., the virtual detector has twice as many rows as the original detector. In the constant-pitch comparison, the number of detector rows was kept constant. During back-projection, bi-linear interpolation was used.

TABLE III. Noise level in the center of rotation. It was determined as the standard deviation in a circular region of interest with a 15 mm diameter located in the center of the field of view. The assumed primary x-ray flux was 10^6 photons per mm^2 and acquisition.

	Constant-γ		Constant-pitch	
Method	16-rows	40-rows	16-rows	40-rows
ASSR	13.5 HU	22.0 HU	13.5 HU	21.9 HU
PI	13.6 HU	22.2 HU	13.9 HU	22.5 HU
PI-SLANT	13.6 HU	22.3 HU	13.9 HU	22.6 HU
3-PI	8.1 HU	12.6 HU	8.1 HU	12.6 HU

For all reconstructions with ASSR, most reconstruction parameters are chosen as recommended by Kachelrieß *et al.*,[10] i.e., linear interpolation in the radial, angular, and z-direction was used. The oversampling parameter w was set to 5 providing the maximum image quality. The attachment angle α^* was chosen to be 60°. Finally, the over-scan parameter f was chosen to be maximal for the 16-row scanner and the chosen pitch. This maximum value is 0.51, resulting in 14 additional projections. [The over-scan parameter f is slightly smaller than the value proposed by Kachelrieß. We also checked the results of choosing the proposed value ($f=0.52$) for the 40-row scanner and found no significant difference in the resulting image quality.] The z-filter parameter $\overline{z}$ was chosen empirically such that in the center of rotation, the same slice thickness as for the other methods was realized. We obtained $\overline{z}=0.5$ mm for the 16-row scanner and $\overline{z}=0.21$ mm for the 40-row scanner; see Sec. III A. During back-projection, linear interpolation was used.

A. Slice sensitivity profiles

The slice sensitivity profile (SSP) was determined using a coin shaped object of 5 mm diameter and 50 μm thickness located on the rotation axis. Four other coins are placed 120 mm off-center on the x- and y-axis. The five positions are called center, east, north, west, and south. The oversampling on the focal spot and on the detector was chosen such that this small object is sampled adequately: For the 16-row scanner, 3×20 was used, and 3×8 for the 40-row scanner, respectively. Figure 5 shows the resulting SSP for the 40-row scanner and Table II summarizes the effective slice thicknesses (full width at half maximum, FWHM). All methods produce almost the same SSP in the center of rotation. There are minor differences in the off-center SSPs: Some of the

TABLE IV. Detector area utilization f of the different methods.

Method	Constant-γ	Constant-Pitch
ASSR	80.4%	29.5%
PI/PI-SLANT	79.3%	29.1%
3-PI	87.2%	87.2%

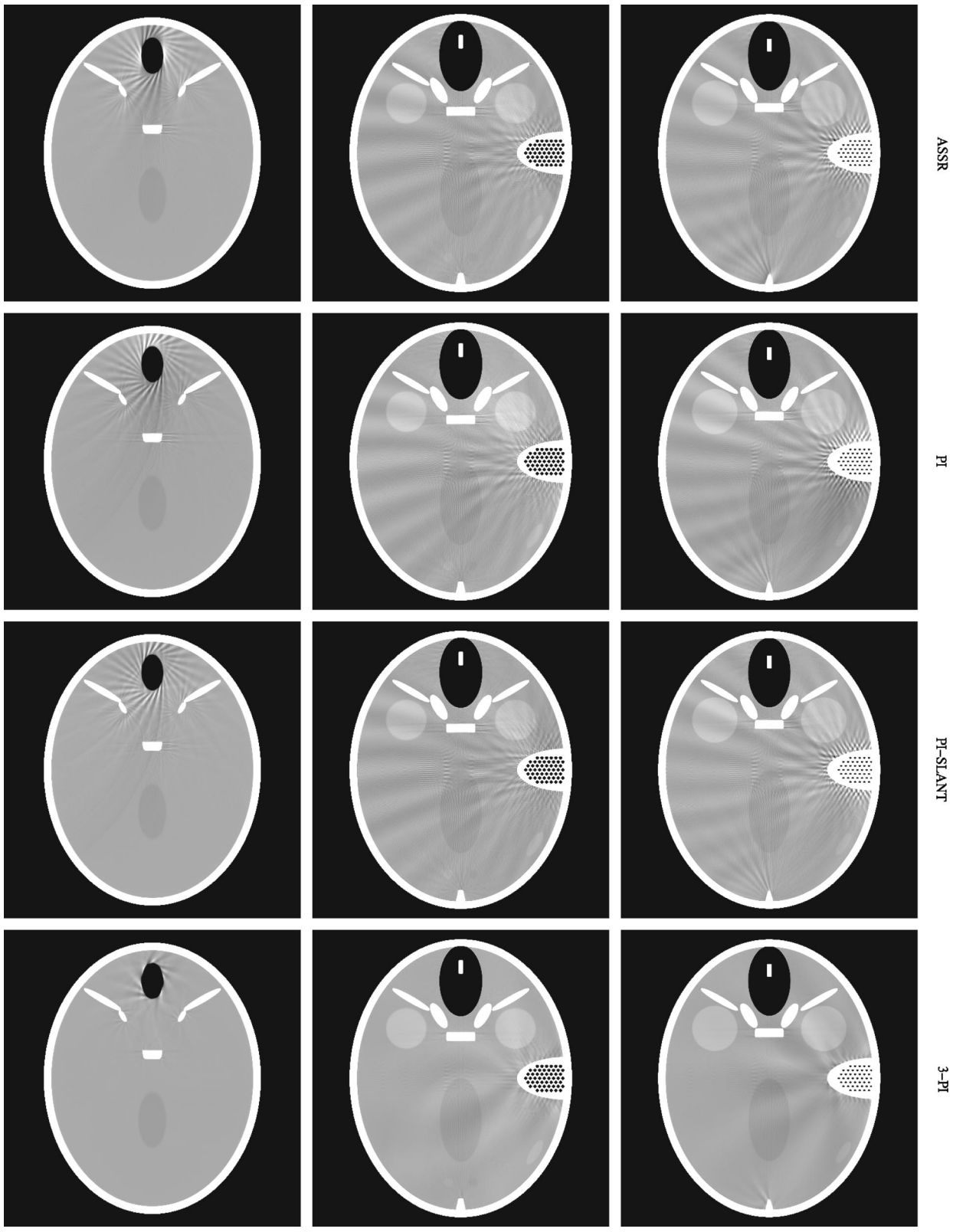

FIG. 8. A constant-γ comparison for the 16-row scanner. The columns correspond to z positions $z_R = -27$ mm, 0 mm, and 5.5 mm. From top to bottom: ASSR, PI, PI-SLANT, 3-PI.

off-center SSPs obtained with ASSR are slightly displaced and broadened. The effect is strongly reduced in the constant-pitch comparison, where the inherent geometrical error is reduced by a factor of 3 due to the smaller pitch. For the 16-row scanner, the differences between the methods are even smaller, and therefore, the results are not shown.

The effective slice thickness is 1.9 mm for the 16-row scanner and 0.75 mm for the 40-row scanner.

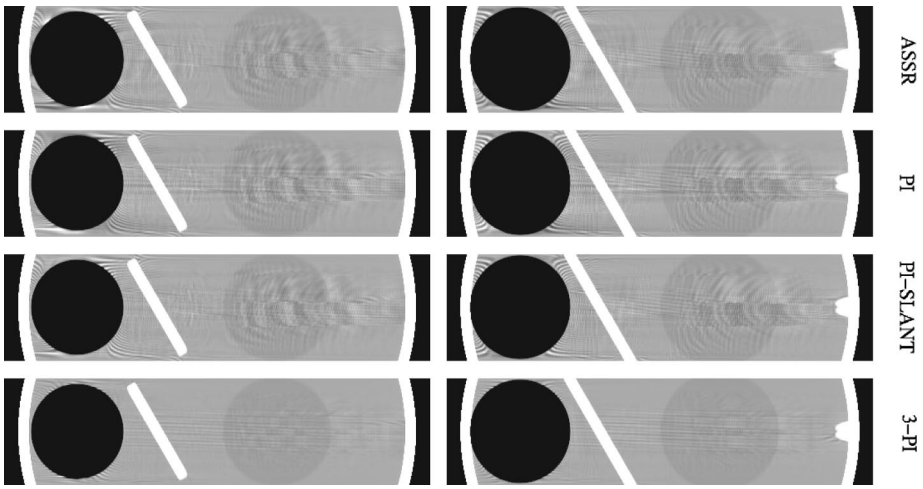

FIG. 9. A constant-γ comparison for the 16-row scanner. Saggital cross sections at $x=-7.75$ mm (left) and $x=+2.75$ mm (right) of the reconstruction results from the 16-row scanner. From top to bottom: ASSR, PI, PI-SLANT, 3-PI.

B. In-plane point spread function

The in-plane point spread function (PSF) was determined using an object which consists of a mathematical line located at the *z*-axis (this results in a projection which is proportional to $1/\cos\gamma$ (γ is the cone-angle) for the column onto which the rotation axis is projected and zero elsewhere). Reconstruction was performed on a grid $256\times1\times256$ containing the rotation axis. The field of view was 10 mm in the *x*-direction and *P* in the *z*-direction. To calculate the in-plane PSF, the average in the *z*-direction was calculated to remove helical artifacts which are present due to the asymmetry induced by the quarter detector offset. The resulting in-plane PSF for the 16-row scanner and the constant-γ comparison is shown in Fig. 6. All algorithms perform equally. As the object is constant in the *z*-direction, the same holds true for the 40-row scanner and for the constant-pitch comparisons.

From a mathematical point of view, all methods are exact for objects which are homogenous in the *z*-direction. As the impact of the slight asymmetry of the acquisition system was removed by averaging, the resulting in-plane PSF should be the same as for a single line CT system with the same column pitch. In fact, such a system produces exactly the same PSF if a filtered back-projection algorithm is used for reconstruction.

C. Noise characteristics and dose utilization

The noise characteristics were determined by the following procedure: A cylindrical object with 0 HU served as an object. Poisson distributed noise was added to the simulated x-ray intensities. We assumed a primary flux of 10^6 photons per mm^2 on the detector and per acquisition. After reconstruction of a slice with 0.5 mm pixel size, the noise level was estimated by calculating the standard deviation within circles of 15 mm radius located at the rotation axis. Table III summarizes the results. All short scan methods have almost the same noise level. The results of the 3-PI method and the short scan methods differ by nearly a factor of $\sqrt{3}$, as expected. The results of the 16-row scanner and the 40-row scanner differ by nearly a factor of 2.5, as expected from the differences in the slice thickness of the two scanners.

One of the main requirements for algorithms in medical applications is that all available data must be used, hence noise has to be as small as possible for any given dose applied. Thus, we will estimate the dose that was applied in this noise study. Figure 7 shows the detector area that is actually used by the different methods in the constant-γ comparison for the detector geometry used in this paper. All short-scan methods use almost the same detector area. The actual percentages of the used detector area for the different methods are summarized in Table IV. We would like to stress the fact that the detector area outside the indicated area is not used at all. Consequently, it can be easily achieved by static collimation, that only the used detector area is irradiated. Of course, this holds also true for the constant-pitch comparison, where the short-scan methods use only 30% of the detector area. We assume that this collimation will be done in a clinical application. Apart from the beginning and end of the helix, each rotation of the gantry increases the field of view in the *z*-direction that can be reconstructed by the pitch. Since the dose applied depends linearly on the number of rotations and the detector utilization *f*, the applied dose depends linearly on f/P. As a matter of fact, this quantity is exactly three times larger for the 3-PI method than for PI and PI-SLANT for both, the constant-γ and the constant-pitch comparison. Thus, we conclude that all methods fulfill the beforementioned requirement for medical applications.

D. Image quality

The forbild head phantom (as given in www.imp.uni-erlangen.de/forbild) was used for the evaluation of the image quality obtained by the different algorithms. The objects designed for resolution measurement were omitted. From a theoretical point of view, all reconstruction algorithms under consideration are exact for objects which are homogeneous along the rotation axis. Therefore, problems are expected especially, if strong gradients in the *z*-direction occur. The forbild head phantom has several strong gradients in the *z*-direction and is thus well suited for testing the algorithms.

For the 40-row scanner with isotropic resolution, a 3×3 oversampling was performed on every pixel and the focal

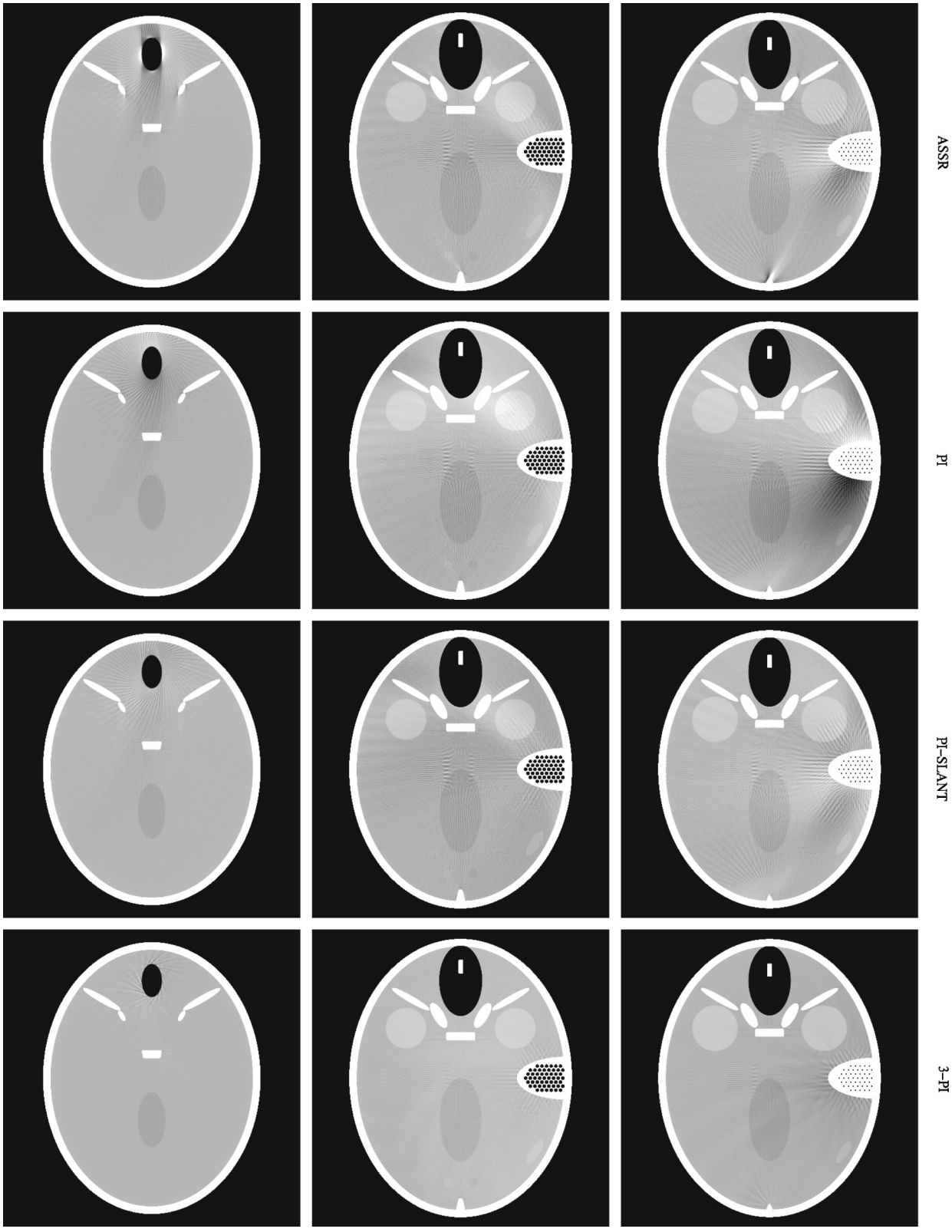

FIG. 10. A constant-γ comparison for the 40-row scanner. The columns correspond to z positions $z_R = -27$ mm, 0 mm, and 5.5 mm. From top to bottom: ASSR, PI, PI-SLANT, 3-PI.

spot. For the 16-row scanner, a 3×7 oversampling was performed, which corresponds to nearly the same density of the rays used for the oversampling.

First, we will focus on the constant-γ comparison: Fig. 8 shows some reconstructed axial slices and Fig. 9 some saggital cross sections for the 16-row scanner. The corresponding results for the 40-row scanner are shown in Figs. 10 and 11.

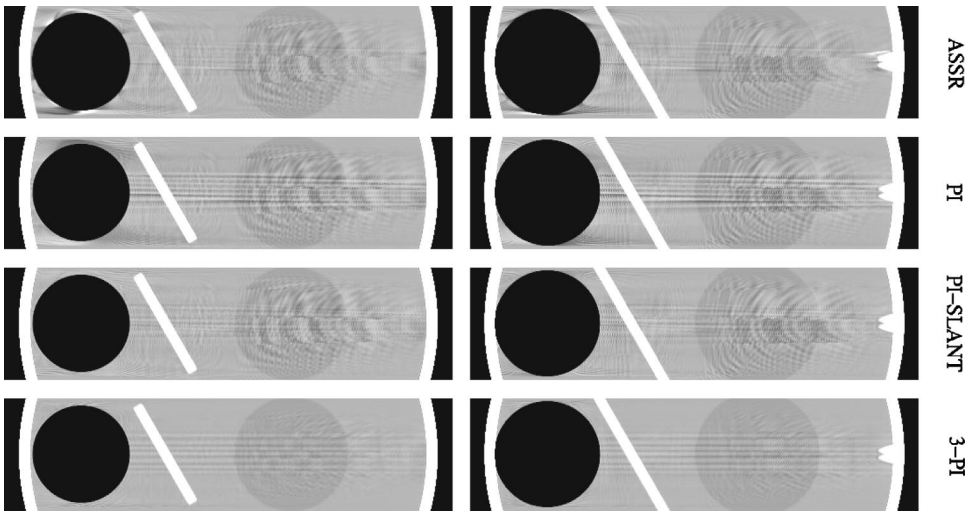

FIG. 11. A constant-γ comparison for the 40-row scanner. Saggital cross sections at $x=-7.75$ mm (left) and $x=+2.75$ mm (right) of the reconstruction results from the 40-row scanner. From top to bottom: ASSR, PI, PI-SLANT, 3-PI.

According to the documentation of the phantom, we refer to the dark sphere in the upper part of the images in Figs. 8 and 10 as to frontal sinus, the bone structure containing several air bubbles in the right as to the inner ear, and finally to the white cone in the lower part as to the petrous bone. All images are displayed with a level of 35 HU and a window of 100 HU.

For the 16-row scanner, ASSR, PI, and PI-SLANT perform almost identically. They produce prominent artifacts which have a wave-like structure in *xy*-planes and a high frequency in the *z*-direction; see Figs. 8 and 9. These waves rotate in the *xy*-plane when the reconstructed slices are viewed in a movie mode. Furthermore, streaks originate from the inner ear; see the right column of Fig. 8. Apart from these common artifacts, ASSR produces a small dark shadow on the left hand side and a bright shadow on the right hand side of the petrous bone at $z=5.5$ mm and some artifacts at the top and the bottom of the frontal sinus. Both are not present in PI and PI-SLANT. PI produces a slight dark shadow below the inner ear which is not present in ASSR and PI-SLANT. The 3-PI method produces also wave-like structures, which are located closer to the neighborhood of the object part which caused them.

The transition from 16 rows to 40 rows results in the following changes (Please note that due to the increased *z*-resolution, the partial volume effect is reduced. This results, e.g. in a ''smaller'' petrous bone at $z=5.5$ mm in Fig. 10 compared with Fig. 8.) Some artifacts are reduced or even disappear, others become stronger, and some remain at almost the same level.

(1) There are some low frequency artifacts present in the saggital cross section which look almost identical for ASSR, PI, and PI-SLANT and are at the same level for both scanners; see Figs. 9 and 11. They correspond to the high frequency in-plane artifacts. The intensity of this type of artifacts appears to be slightly higher for PI and PI-SLANT than for ASSR. If linear interpolation is used in the parallel rebinning step for these methods instead of 6th order Lagrangian, the artifact levels become the same.
(2) For each method, the low frequency in-plane waves are reduced; see Figs. 8 and 10. Correspondingly, many of the high frequency artifacts, which were present in the saggital cross sections in Fig. 9, are reduced. See in particular the region around the frontal sinus shown in Fig. 11.
(3) Some artifacts recognized in the results of the 16-row scanner become now more prominent, namely, a streak emanates from the petrous bone in the ASSR result at $z=5.5$ mm; see the right column of Fig. 10. This streak is also visible in the saggital cross sections; see the right column of Fig. 11. The badly resolved border between the frontal sinus and the surrounding tissue in the ASSR result, and the shadow behind the inner ear in the PI result; see the right column of Fig. 10. Some stronger shadows are present in other slices of the PI result which correspond to the horizontal streaks visible in the saggital cross section shown in Fig. 11. Again, these artifacts are not present in the PI-SLANT method and ASSR.

Now we focus on the constant-pitch comparison: Results for the 16-row scanner are shown in Figs. 12 and 13 and for the 40-row scanner in Figs. 14 and 15. For the 16-row scanner, the dominant in-plane wave-like artifacts which have different wavelengths in the constant-γ comparison are now synchronous for all methods; see Figs. 8 and 12. The amplitude is significantly larger for the short-scan methods than for the 3-PI method. Interestingly, the amplitude of the waves is slightly larger for the smaller pitch. This can be seen e.g., in the saggital cross sections, where the almost horizontally oriented streaks are more prominent in the constant-pitch comparison, see Fig. 13, than in the constant-γ comparison, see Fig. 9. There is also a new type of artifact visible in the PI and the PI-SLANT result: An arc extends almost horizontally in the right column of Fig. 13.

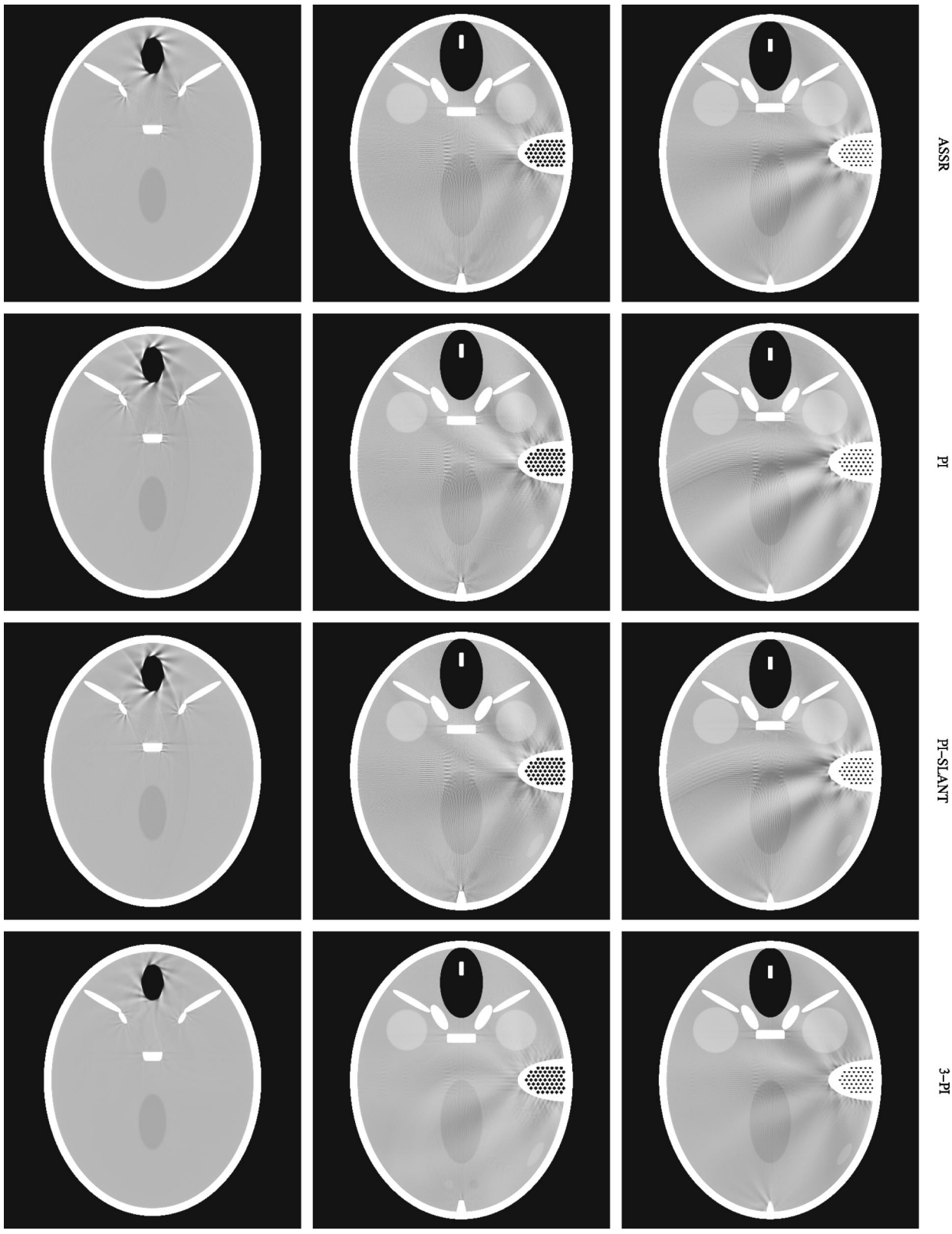

FIG. 12. A constant-pitch comparison for the 16-row scanner. The columns correspond to z positions $z_R = -27$ mm, 0 mm, and 5.5 mm. From top to bottom: ASSR, PI, PI-SLANT, 3-PI.

For the 40-row scanner, the same observation can be made: The in-plane waves which can be seen in the short-scan results, e.g., around the frontal sinus in the left column of Fig. 10, become synchronous to the waves visible in the 3-PI result. Again, the amplitude is larger for the short-scan methods. Most of the artifacts which are different for the short-scan methods in the constant-γ comparison are not visible in the constant-pitch comparison. Still, the boundary of

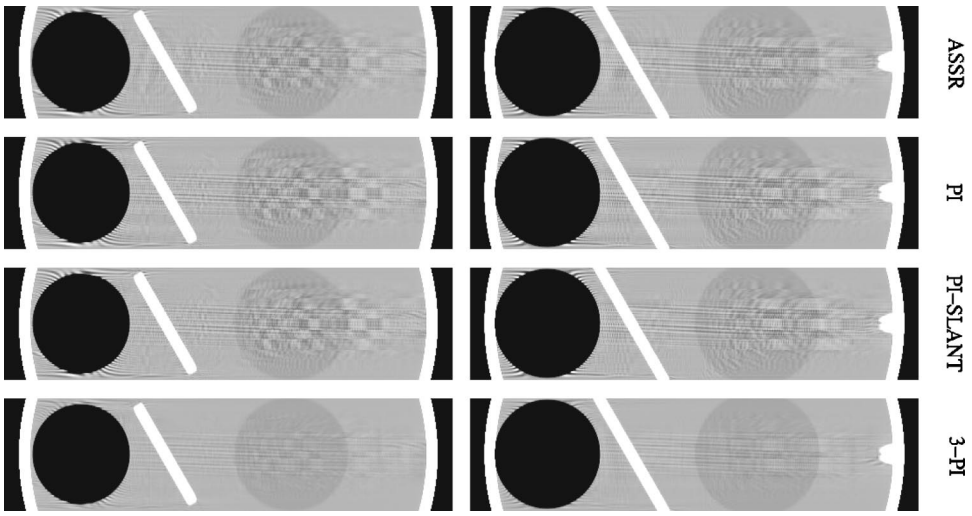

FIG. 13. A constant-pitch comparison for the 16-row scanner. Saggital cross sections at $x=-7.75$ mm (left) and $x=+2.75$ mm (right) of the reconstruction results from the 16-row scanner. From top to bottom: ASSR, PI, PI-SLANT, 3-PI.

the frontal sinus is sometimes not appropriately resolved by ASSR; see the left column of Fig. 15.

By comparing the two constant-pitch studies, we notice again that the dominant wave-like artifacts visible in the 16-row scanner, are strongly reduced if the 40-row scanner is used. In general we observe that the waves get a higher in-plane frequency if the z-sampling on the detector is increased; compare Fig. 8 with 10 and Fig. 12 with 14. On the other hand, their frequency is reduced if the pitch is reduced; compare Fig. 8 with 12 and Fig. 10 with 14.

To complete the study, Fig. 16 shows an example of the constant-dose comparison for the 16-row scanner. It is assumed that the number of projections per turn is increased by a factor of three compared to the constant-γ comparison. Only the PI-SLANT result is shown. As expected, there is hardly any difference compared with the constant-γ case. The same holds true for the other short-scan methods.

IV. DISCUSSION

All methods investigated in this study employ a parallel rebinning followed by a filtered back-projection. Thus, we do not expect any differences in the in-plane resolution of the different algorithms. This is in perfect agreement with our results. The difference in the interpolation, i.e., the use of higher order Lagrangian interpolation in the angular and radial direction for the PI-methods, does not affect the result because the re-binned detector spacing is chosen in such a way that the detector columns of the original and the virtual detector match in the center.

The design of the study allows to identify the most prominent in-plane artifacts for the 16-row scanner as some kind of aliasing in the z-direction. They disappear almost completely, if a finer z-sampling on the detector is used. The 3-PI method is far less sensitive to this z-aliasing. By using a three times longer illumination, features of the object in the z-direction are sampled three times with different rasters and also from opposite directions. This suppresses aliasing similar to the well known suppression of in-plane aliasing by the use of a quarter detector shift. This inference is also supported by the constant-pitch comparison. It is clearly shown that the structure of the artifacts is induced by the pitch and the discrete z-sampling on the detector. The 3-PI method is also less sensitive to in-plane aliasing, because it can profit from the quarter detector shift, while the other methods cannot.

A significant amount of artifacts visible in the saggital cross section in Figs. 9 and 11 are clearly due to in-plane aliasing. However, some of the artifacts are stronger for PI and PI-SLANT if higher order interpolation is used during rebinning (as shown in the results) but are at the same level if linear interpolation is used. Typically, higher order interpolation is less sensitive to aliasing than linear interpolation. Furthermore, it provides typically a smaller in-plane PSF, thus it can recover sharp objects better than linear interpolation. Thus, we can conclude that these artifacts are not due to in-plane aliasing, but they are caused by the z-gradients which introduce sharp in-plane features which are recovered better by the use of higher order interpolation.

The results from the 40-row scanner provide good information about the differences in the performance of the algorithms and the origin of the artifacts. ASSR and PI-SLANT perform the filtering on optimized lines, while the PI-method does not. On the other hand, PI and PI-SLANT take the correct 3D acquisition geometry during back-projection into account, while ASSR does not. From the observation that some artifacts are present in the results of PI, namely shadows, but not in results of ASSR and PI-SLANT, we can conclude that these artifacts originate from the worse filter direction. On the other hand, artifacts, which are present only in images reconstructed using ASSR, e.g., streaks, originate from the 2D approximation of the 3D acquisition geometry. These artifacts which become stronger for the 40-row scanner are suppressed in the 16-row scanner due to the larger slice thickness. In Ref. 10, the mean deviation between the real rays and the virtual rays used for reconstruction within the ASSR method is determined to be approximately 1.5% of the pitch. In the constant-γ comparison, this is 0.5 mm and, thus, the mean deviation is approximately the same as the nominal slice thickness. Especially, far away from the rota-

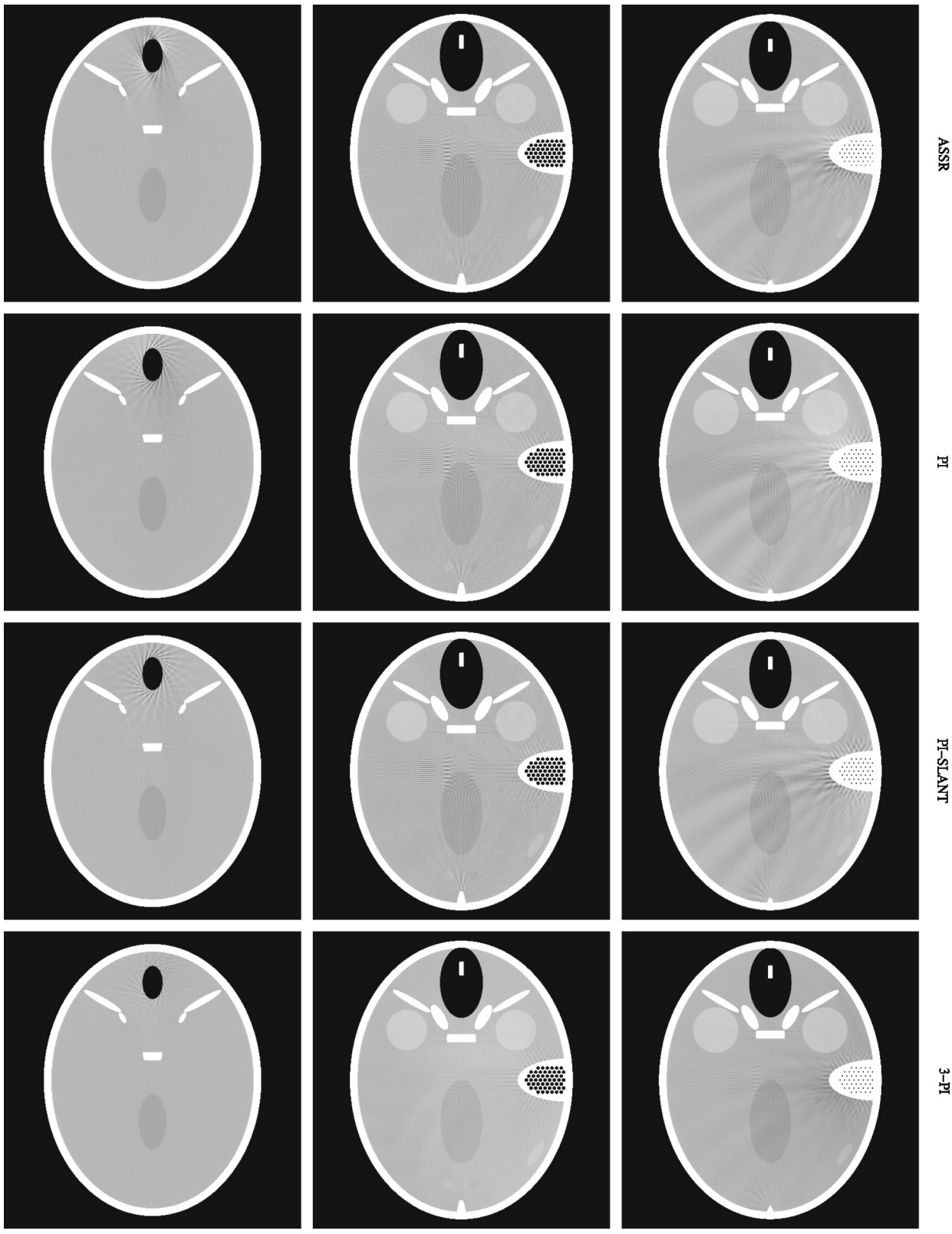

FIG. 14. A constant-pitch comparison for the 40-row scanner. The columns correspond to z positions $z_R = -27$ mm, 0 mm, and 5.5 mm. From top to bottom: ASSR, PI, PI-SLANT, 3-PI.

tion axis, this error is significantly larger for some projection angles. This is consistent with our observation that artifacts which are unique to ASSR are located always far away from the rotation axis.

In a previous study by Bruder *et al.*[20] ASSR performed significantly better than PI, especially for large pitch values, which is not in line with our study. In our opinion, this is due to the following reasons: First of all, in Ref. 20, a detector

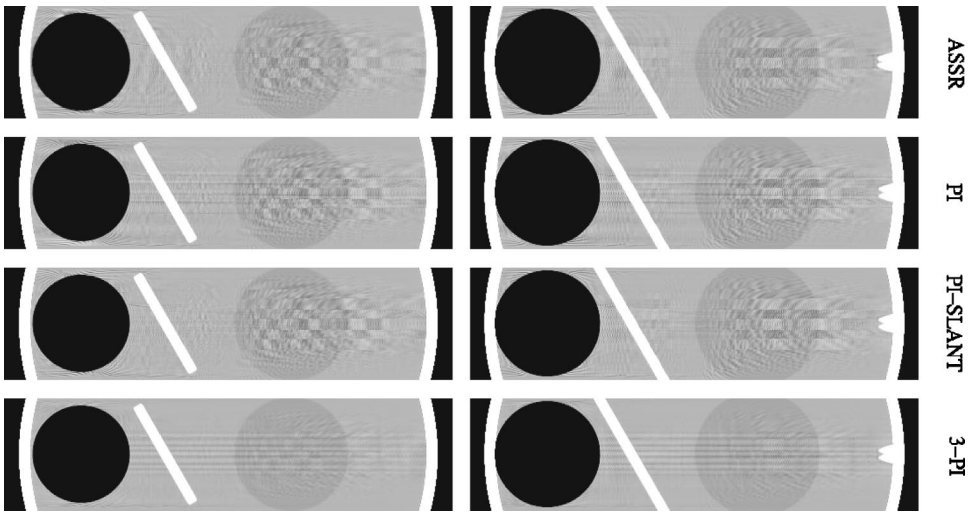

FIG. 15. A constant-pitch comparison for the 40-row scanner. Saggital cross sections at $x=-7.75$ mm (left) and $x=+2.75$ mm (right) of the reconstruction results from the 40-row scanner. From top to bottom: ASSR, PI, PI-SLANT, 3-PI.

which is centered around the rotation axis was used for the PI-method, while a planar detector was used for ASSR. We suspect that this choice is the reason for the significantly lower in-plane resolution and the higher sensitivity to in-plane aliasing of the PI method compared with ASSR. The stronger in-plane aliasing artifacts produced by the PI-method, which are clearly visible in Ref. 20, correspond with the higher artifact level in the coronal and saggital cross sections according to our study. Second, Bruder *et al.* used a *z*-filter width $\overline{z}$ equal to the nominal slice thickness "in order to guarantee highest *z*-resolution." [20] However, it turned out that the PI-method yields a narrower SSP (1.2 times the nominal slice thickness compared to 1.3 times for ASSR). By the mentioned choice of $\overline{z}$, the authors suppressed the aliasing artifacts in the *z*-direction which correspond according to our study to exactly the kind of in-plane artifacts that are shown in Ref. 20. Although the difference between the slice thickness seems to be small, the impact on the in-plane artifact level is quite high. At least in our study, it was possible to achieve the same slice thickness for ASSR and PI by reducing $\overline{z}$ to only 40% of the nominal slice thickness. It is not surprising that artifacts are reduced by choosing the reconstruction parameters in a way that the slice thickness is increased. The same effect can be achieved, if the reconstruction result of the PI or PI-SLANT method is smoothed in *z*-direction hindsight.

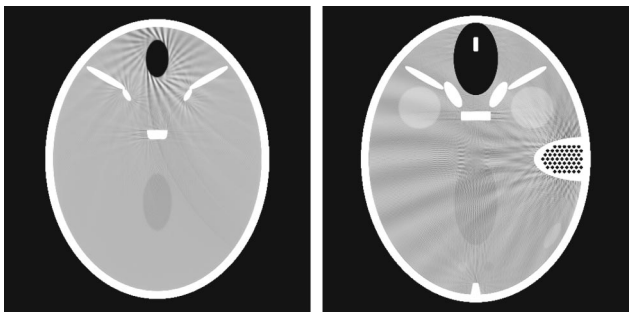

FIG. 16. A constant-dose comparison for the 16-row scanner. It is assumed that the system takes 4320 projections per rotation. Images are reconstructed using the PI-SLANT method. The columns correspond to *z* positions $z_R=-27$ mm and 0 mm.

In the constant-γ comparison, 3-PI performs much better than ASSR and PI for both scanners, and it performs better than PI-SLANT for the 16-row scanner. Both artifacts due to in-plane aliasing and due to *z*-aliasing are efficiently suppressed due to the use of redundant data. Even in the constant-pitch comparison, 3-PI performs better than the other methods although it must handle a three times larger cone-angle. This emphasizes the importance of redundant data to a minimize sampling artifacts. However, it remains unclear why there are no artifacts visible which might be caused by the wrong filter direction. From the results of the PI-method, it might be expected that shadows are produced, but this is not the case. We can only speculate that these shadows, which have a high frequency in *z* for the PI-method, average out by the use of redundant data.

V. SUMMARY

We presented a detailed comparison of four approximate cone-beam reconstruction methods: ASSR, PI, PI-SLANT, and 3-PI. ASSR, PI, and PI-SLANT use only nonredundant data—or only a very small amount of redundant data in the case of ASSR—while the 3-PI method uses a redundancy of three. In order to do a qualitative and quantitative comparison of the artifacts produced by the different methods, we ensured that both the SSP and the PSF are the same for all methods.

By an artifact analysis, we showed that aliasing in the *z*-direction introduces severe in-plane artifacts and *vice versa*. These artifacts are almost identical for ASSR, PI, and PI-SLANT. For a 16-row scanner, ASSR, PI, and PI-SLANT perform almost identically, because the major source of artifacts is aliasing in the *z*-direction. For the 40-row scanner, ASSR and PI produce different types of artifacts: PI tends to produce shadows in *xy*-planes with a high frequency in the *z*-direction, while ASSR produces artifacts with a more complex shape in all directions. PI-SLANT performs signifi-

cantly better than both. Thus, we see a clear benefit from the additional effort of a proper 3D back-projection.

Both kinds of aliasing artifacts present in the PI method are strongly suppressed by the use of redundant data and the use of the 3-PI method. At the same time, no severe artifacts are introduced by the approximate nature of the algorithm, resulting in an image quality which is better than that achieved by any other method. Thus, we conclude that using redundant data has the potential to improve the image quality and that the 3-PI method is an efficient method that can handle them. The constant-pitch comparison showed that the 3-PI method provides better image quality even if the short scan methods operate only at a third of the cone-angle. From a clinical point of view, we see therefore two situations where the 3-PI method could be used: For a high dose application where the x-ray source cannot provide sufficient photons to achieved the desired signal to noise ratio and second for applications where a high image quality at high *z*-resolution is required. For an application where a short scan time is the most important requirement, short-scan methods should be used.

Aliasing in the *z*-direction appears to be the source of most of the in-plane artifacts visible in the nonisotropic 16-row scanner. As the artifact level should not be dominated by a single parameter, namely the height of the detector pixel in our case, we see a need for isotropic detectors.

ACKNOWLEDGMENT

We would like to thank Henrik Turbell for the advice on the PI-SLANT-method.

[a]Electronic mail: thomas.koehler@philips.com

[1] K. Taguchi and H. Aradate, ''Algorithm for image reconstruction in multi-slice helical CT,'' Med. Phys. **25**, 550–561 (1998).
[2] H. Hu, ''Multi-slice helical CT: Scan and reconstruction,'' Med. Phys. **26**, 5–18 (1999).
[3] S. Schaller, T. Flohr, K. Klingenbeck, J. Krause, T. Fuchs, and W. A. Kalender, ''Spiral interpolation algorithm for mulitslice spiral CT–part I: Theory,'' IEEE Trans. Med. Imaging **19**, 822–834 (2000).
[4] H. Kudo, F. Noo, and M. Defrise, ''Cone-beam filtered-backprojection algorithm for truncated helical data,'' Phys. Med. Biol. **43**, 2885–2909 (1998).
[5] H. Kudo, F. Noo, and M. Defrise, ''Quasi-exact reconstruction for long-object problem in helical cone-beam tomography,'' in *Proceedings of the 3D'99 Conference* (Egmond aan Zee, The Netherlands, 1999).
[6] K. C. Tam, F. Sauer, G. Lauritsch, and A. Steinmetz, ''Backprojection spiral scan region-of-interest cone beam CT,'' Proc. SPIE **3661**, 433–441 (1999).
[7] M. Defrise, F. Noo, and H. Kudo, ''A solution to the long object problem in helical cone-beam tomography,'' Phys. Med. Biol. **45**, 623–643 (2000).
[8] G. Larson, C. C. Ruth, and C. R. Crawford, ''Nutating slice CT image reconstruction apparatus and method,'' US Patent 5,802,134, 1998.
[9] D. Heuscher, ''Helical cone beam scans using oblique 2D surface reconstruction,'' in Ref. 5.
[10] M. Kachelrieß, S. Schaller, and W. A. Kalender, ''Advanced single-slice rebinning in cone-beam spiral CT,'' Med. Phys. **27**, 754–772 (2000).
[11] H. Bruder, M. Kachelrieß, S. Schaller, K. Stierstorfer, and T. Flohr, ''Single-slice rebinning reconstruction in spiral cone-beam computed tomography,'' IEEE Trans. Med. Imaging **19**, 873–887 (2000).
[12] S. Schaller, ''Practical image reconstruction for cone-beam computed tomography,'' Ph.D. thesis, University of Erlangen, Germany, 1998.
[13] P. E. Danielsson, P. Edholm, J. Eriksson, M. Magnusson-Seger, and H. Turbell, ''The original pi-method for helical cone-beam ct,'' in Ref. 5.
[14] H. Turbell, ''Cone-beam reconstruction using filtered backprojection,'' Tech. Rep. Thesis No. 672, Linköping University, 2001.
[15] R. Proksa, T. Köhler, M. Grass, and J. Timmer, ''The *n*-PI-method for helical cone-beam CT,'' IEEE Trans. Med. Imaging **19**, 848–863 (2000).
[16] S. Schaller, K. Stierstorfer, H. Bruder, M. Kachelrieß, and T. Flohr, ''Novel approximate approach for high quality image reconstruction in helical cone-beam CT at arbitrary pitch,'' Proc. SPIE. **4322**, 113–127.
[17] P. E. Danielsson, P. Edholm, J. Eriksson, and M. Magnusson-Seger, ''Towards exact 3D-reconstruction for helical cone-beam scanning of long objects,'' in *Proceedings of the 3D'97 Conference*, Nemacolin, Pennsylvania, 1997.
[18] H. Turbell, ''Three-dimensional image reconstruction in circular and helical computed tomography,'' Tech. Rep. Lic. Thesis No. 760, Linköping University, 1999.
[19] W. Kalender, *Computed Tomography: Fundamentals, System Technology, Image Quality, Applications* (Publics MCD-Verlag, Munich, 2000).
[20] H. Bruder, M. Kachelrieß, S. Schaller, and T. Mertelmeier, ''Performance of approximate cone-beam reconstruction in multi-slice computed tomography,'' Proc. SPIE **3979**, 541–553 (2000).